

# UC Berkeley

## UC Berkeley Previously Published Works

### Title

CO<sub>2</sub> reduction on pure Cu produces only H<sub>2</sub> after subsurface O is depleted: Theory and experiment

### Permalink

<https://escholarship.org/uc/item/3555m2z1>

### Journal

Proceedings of the National Academy of Sciences of the United States of America, 118(23)

### ISSN

0027-8424

### Authors

Liu, Guiji  
Lee, Michelle  
Kwon, Soonho  
et al.

### Publication Date

2021-06-08

### DOI

10.1073/pnas.2012649118

Peer reviewed



# CO<sub>2</sub> reduction on pure Cu produces only H<sub>2</sub> after subsurface O is depleted: Theory and experiment

Guiji Liu<sup>a,b,c,1</sup>, Michelle Lee<sup>a,b,d,1</sup>, Soonho Kwon<sup>e,f,g,1</sup>, Guosong Zeng<sup>b,c</sup>, Johanna Eichhorn<sup>a,b,h,i</sup>, Aya K. Buckley<sup>a,b,j</sup>, F. Dean Toste<sup>a,j</sup>, William A. Goddard III<sup>e,f,g,2</sup>, and Francesca M. Toma<sup>a,b,c,2</sup>

<sup>a</sup>Joint Center for Artificial Photosynthesis, Lawrence Berkeley National Laboratory, Berkeley, CA 94720; <sup>b</sup>Chemical Sciences Division, Lawrence Berkeley National Laboratory, Berkeley, CA 94720; <sup>c</sup>Liquid Sunlight Alliance, Lawrence Berkeley National Laboratory, Berkeley, CA 94720; <sup>d</sup>Department of Chemistry and Chemical Biology, Cornell University, Ithaca, NY 14853; <sup>e</sup>Materials and Process Simulation Center, California Institute of Technology, Pasadena, CA 91125; <sup>f</sup>Joint Center for Artificial Photosynthesis, California Institute of Technology, Pasadena, CA 91125; <sup>g</sup>Liquid Sunlight Alliance, California Institute of Technology, Pasadena, CA 91125; <sup>h</sup>Walter Schottky Institut, Technische Universität München, 85748 Garching, Germany; <sup>i</sup>Physik Department, Technische Universität München, 85748 Garching, Germany; and <sup>j</sup>Department of Chemistry, University of California, Berkeley, CA 94720

Edited by Michael L. Klein, Temple University, Philadelphia, PA, and approved April 13, 2021 (received for review June 18, 2020)

**We elucidate the role of subsurface oxygen on the production of C<sub>2</sub> products from CO<sub>2</sub> reduction over Cu electrocatalysts using the newly developed grand canonical potential kinetics density functional theory method, which predicts that the rate of C<sub>2</sub> production on pure Cu with no O is ~500 times slower than H<sub>2</sub> evolution. In contrast, starting with Cu<sub>2</sub>O, the rate of C<sub>2</sub> production is >5,000 times faster than pure Cu(111) and comparable to H<sub>2</sub> production. To validate these predictions experimentally, we combined time-dependent product detection with multiple characterization techniques to show that ethylene production decreases substantially with time and that a sufficiently prolonged reaction time (up to 20 h) leads only to H<sub>2</sub> evolution with ethylene production ~1,000 times slower, in agreement with theory. This result shows that maintaining substantial subsurface oxygen is essential for long-term C<sub>2</sub> production with Cu catalysts.**

electrocatalysis | hydrogen evolution reaction | ethylene evolution | grand canonical potential kinetics | DFT

Anthropogenic carbon emissions, particularly CO<sub>2</sub>, are surging primarily because of global fossil fuel consumption, raising serious environmental concerns about global warming (1). Recycling CO<sub>2</sub> via electrochemical (EC) reduction of carbon dioxide (CO<sub>2</sub>RR) to fuels and valuable chemicals using renewable energy could play an important role in global efforts to address current energy demand and climate challenges (2). CO<sub>2</sub> can be electrochemically reduced to C<sub>1</sub> products (CO, methane, and formic acid), C<sub>2</sub> products (ethylene, ethane, and ethanol), and C<sub>3</sub> products (*n*-propanol) (3, 4). The major challenge to make this process economically viable is to increase selectivity to generate higher-hydrocarbon products.

In this context, copper (Cu) remains the only single metal capable of producing significant amounts of higher hydrocarbons, such as C<sub>2</sub> products ethylene or ethanol. Indeed, many experiments report that oxide-derived Cu catalysts lead to higher activity for C<sub>2</sub> products (5–8). However, the role of oxygen in the Cu catalyst and the correlation with the underlying C<sub>2</sub> production mechanism remains a subject of considerable debate (4). We suggested earlier that the optimum catalyst is the partially reduced cuprous oxide (Cu<sub>2</sub>O) surface in which surface and/or subsurface oxygen of Cu<sub>2</sub>O are adjacent to a reduced Cu<sup>0</sup> surface, termed MEOM for metal embedded in oxidized matrix (9). Density functional theory (DFT) calculations on model systems showed that MEOM leads to a barrier for CO<sub>2</sub> reduction to CO that is 0.22 eV lower than for pure Cu<sup>0</sup> and to a barrier for CO dimerization (the first step toward C<sub>2</sub> products) that is 0.39 eV lower than for pure Cu<sup>0</sup>. This result suggests that C<sub>2</sub> production on the MEOM surface could be >5,000 times faster than for pure Cu<sup>0</sup>. Indeed, other groups have recently hypothesized that surface Cu<sup>+</sup> and/or subsurface oxygen on Cu might play an essential role in promoting CO dimerization and ethylene production (10–14). However, others have argued that such surface or subsurface oxygen species cannot be important because many experiments show that surface oxygen is rapidly

depleted under CO<sub>2</sub>RR conditions (15, 16), and it is, rather, suggested that surface roughness plays an active role in bolstering ethylene selectivity (16, 17). Hence, fundamental understanding into the relationship between the presence of oxygen and the increased C<sub>2</sub> production activity on Cu catalyst can solve the existing debates.

Here, we combine theory and experiments to disentangle the contributions from both Cu that contains oxygen and fully reduced (or depleted) Cu<sup>0</sup> to uncover the role of subsurface oxygen in promoting C–C coupling and consequently C<sub>2</sub> production on Cu catalysts. We predict that hydrogen evolution reaction (HER) on pure Cu(111) leads to a turnover frequency (TOF) = 0.32/s, in stark contrast to C<sub>2</sub> production, which we predict to have a TOF = 0.0006/s, which is ~500 times slower than HER. Our time course experiments confirm these predictions, showing that, when continuing CO<sub>2</sub> reduction for times up to 20 h, the C<sub>2</sub> production rates decrease to a level of 1,600 and 680 times slower than HER on polycrystalline Cu and Cu<sub>2</sub>O catalysts, respectively.

In contrast, starting with Cu<sub>2</sub>O, we find that the reduction leads to a Cu<sup>0</sup>/Cu<sub>2</sub>O structure, with a thin, disordered Cu<sup>0</sup> surface on top of the Cu<sub>2</sub>O substrate. We calculate that this structure leads to TOF = 3.95/s for C<sub>2</sub> production compared to TOF = 10.02/s for HER, which is 2.58 times faster. This result is consistent with our experiments, which find HER production to be 2.1 times higher than C<sub>2</sub> during the first 5 h. In addition, we predict that C<sub>2</sub> production on the Cu<sup>0</sup>/Cu<sub>2</sub>O model is a factor of 5,000 times faster

## Significance

**Electrochemical reduction of CO<sub>2</sub> to fuels and valuable chemicals is a global imperative to address energy and climate challenges. Despite enormous efforts, there is not yet a commercial process. The best catalyst remains Cu metal, but a great deal of controversy revolves around the role of the presence of oxygen in the material. We combine theory and experiments to show that pure Cu without subsurface oxygen leads to no organic products. Thus, maintaining substantial oxygen at Cu surfaces is essential for long-term reduction of CO<sub>2</sub> to organics.**

Author contributions: G.L., M.L., S.K., F.D.T., W.A.G., and F.M.T. designed research; G.L., M.L., S.K., and G.Z. performed research; J.E. and A.K.B. performed preliminary measurements; G.L., M.L., S.K., W.A.G., and F.M.T. analyzed the data; and G.L., M.L., S.K., F.D.T., W.A.G., and F.M.T. wrote the paper.

The authors declare no competing interest.

This article is a PNAS Direct Submission.

Published under the PNAS license.

<sup>1</sup>G.L., M.L., and S.K. contributed equally to this work.

<sup>2</sup>To whom correspondence may be addressed. Email: wagoddard3@gmail.com or fmtoma@lbl.gov.

This article contains supporting information online at <https://www.pnas.org/lookup/suppl/doi:10.1073/pnas.2012649118/-DCSupplemental>.

Published June 3, 2021.

than that on pure Cu(111). Indeed, our experiments measured an initial partial current density of ethylene production on Cu<sub>2</sub>O of 0.6 to ~0.8 mA/cm<sup>2</sup>, which becomes negligible after 20 h on fully depleted Cu (~1/1,000 of the H<sub>2</sub> current).

These calculations of TOF as a function of applied potential (U) use our recently developed grand canonical potential kinetics (GCP-K) methodology that predicts the evolution of the reaction intermediates and transition states (TSs) in solvent to obtain the TOF as a function of U (18). In this approach, the solvated structures and energetics of the intermediates adjust adiabatically as the U is changed, leading to very accurate rates versus U. Here, we apply GCP-K to directly assess the impact of subsurface oxygen on the C<sub>2</sub> production over Cu catalysts. Many theoretical studies have been reported on the product distribution during CO<sub>2</sub>RR, but nearly all were carried out for fixed charge, usually zero. None have previously considered optimizing structure and kinetic activation energies as a function of U (19–23). In this study, we consider all thermodynamically stable structures of Cu<sub>2</sub>O using GCP-K DFT calculations at U = -1 V<sub>RHE</sub> with pH 7, common experimental conditions for examining the activity of Cu-

based catalysts in CO<sub>2</sub>RR (6, 17). Here, the U is U = -1 V on the reversible hydrogen electrode (RHE) scale. The GCP-K formulation allows the geometries to relax as U is changed so that the microkinetics allows all structures (equilibrium states and saddle points for TSs) to remain optimum for each U. This development enables us to track the free energy continuously with U at a computational cost close to conventional canonical DFT calculations (see *SI Appendix* for further details of GCP-K method, *SI Appendix*, Figs. S1 and S2).

First, we performed GCP-K calculations to construct the surface Pourbaix diagram shown in Fig. 1A. Starting from intact Cu<sub>2</sub>O(111), we gradually reduced the surface by removing various numbers of oxygen and plotted the free energies of eight states (*SI Appendix*, Fig. S3 and Table S1), as a function of U. The results show that the disordered Cu<sup>0</sup>/Cu<sub>2</sub>O surface is more stable at -1 V<sub>RHE</sub> than the MEOM and Cu<sub>2</sub>O models. Therefore, we considered the Cu<sup>0</sup>/Cu<sub>2</sub>O model as the structure for Cu<sub>2</sub>O at -1 V<sub>RHE</sub>. We assume for the pure Cu with no O that the catalyst relaxes back to Cu(111) (*SI Appendix*, Fig. S4), using this as the model for fully depleted Cu<sub>2</sub>O or Cu. We consider the MEOM surface for comparison in

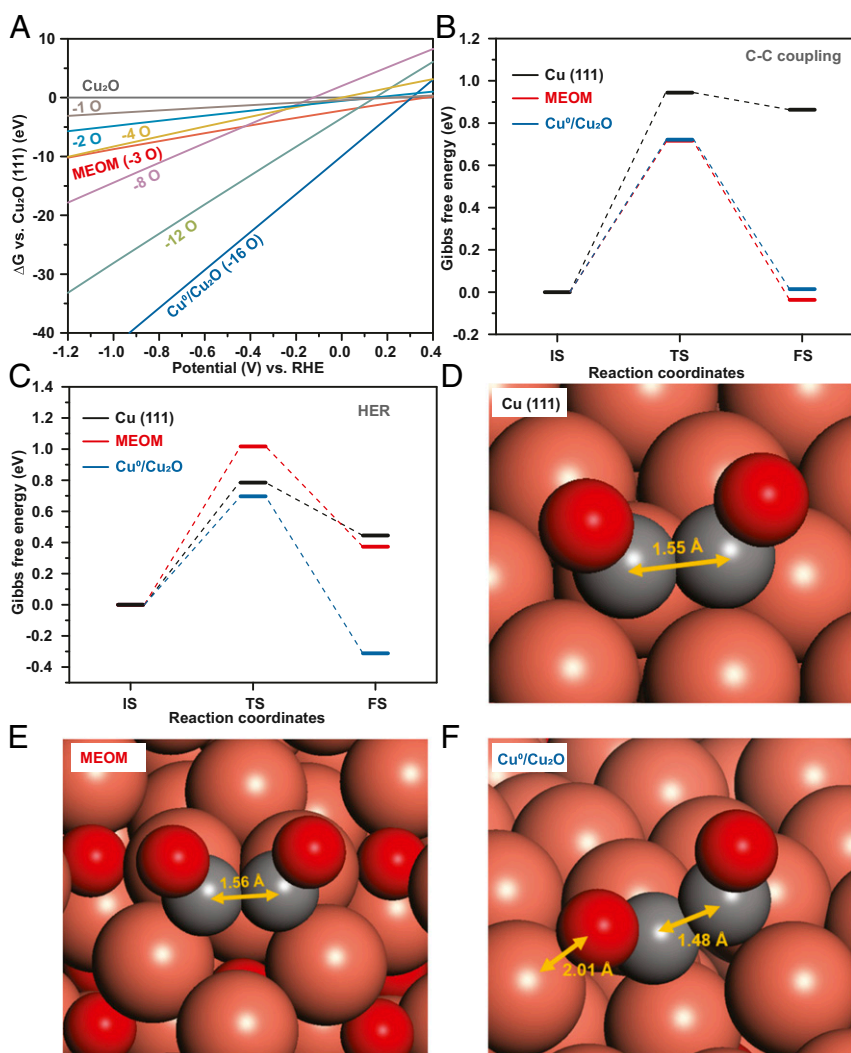


**Fig. 1.** GPC-K DFT calculations for different Cu phases and their relation to C<sub>2</sub> production. Surface free energies as a function of U of various surface phases with different numbers of reduced lattice oxygen potential energy surfaces for the CO dimerization (A), the RDS for C<sub>2</sub> production (B), and the RDS for HER at U = -1 V<sub>RHE</sub> and pH 7 on Cu(111), MEOM, and Cu<sup>0</sup>/Cu<sub>2</sub>O (C). The RDS are the Heyrovsky step [H<sub>ad</sub>+H<sub>2</sub>O(l) + e<sup>-</sup> → H<sub>2</sub>(g) +OH<sup>-</sup>(aq)] for Cu(111) and MEOM and the Volmer step [H<sub>2</sub>O(l) + e<sup>-</sup> → H<sub>ad</sub>+ OH<sup>-</sup>(aq)] for Cu<sup>0</sup>/Cu<sub>2</sub>O. OCCO\* geometries on Cu(111) (D), OCCO\* geometries on MEOM (E), and OCCO\* geometries on Cu<sup>0</sup>/Cu<sub>2</sub>O catalysts (F). The U<sub>s</sub> for each state correspond to -1.25 V<sub>RHE</sub>, -1.15 V<sub>RHE</sub>, and -1.02 V<sub>RHE</sub>, respectively. The C–C bond distances are indicated for all catalysts, and Cu–O bond distance is also indicated for Cu<sup>0</sup>/Cu<sub>2</sub>O catalysts.

**SI Appendix.** We predicted the free energy barriers for HER and for CO dimerization (the dominant step in C<sub>2</sub> formation) for these models.

Our previous full solvent quantum mechanics molecular dynamics studies showed that C–C coupling of two surface CO is the rate determining step (RDS) for producing C<sub>2</sub> products (24). We predict that the  $\Delta G^\ddagger = 0.72$  eV for C–C coupling on the disordered Cu<sup>0</sup>/Cu<sub>2</sub>O surface (Fig. 1B) led to TOF = 3.95/s, which is 5,840 times faster than our predicted to  $6.77 \times 10^{-4}$ /s for oxygen depleted Cu(111) surface, which has a barrier of  $\Delta G^\ddagger = 0.94$  eV [close to our previous results (9)]. This enhancement of C–C coupling on Cu<sup>0</sup>/Cu<sub>2</sub>O is attributed to its capability of forming a (OCC)O–Cu bond, which greatly stabilizes OCCO\*, as shown in Fig. 1F and SI Appendix, Fig. S3.

For HER, we considered the following:

- Volmer [H<sub>2</sub>O(l) + e<sup>-</sup> → H<sub>ad</sub>+OH<sup>-</sup>(aq)] step and
- Heyrovsky [H<sub>ad</sub>+H<sub>2</sub>O(l) + e<sup>-</sup> → H<sub>2</sub>(g) +OH<sup>-</sup>(aq)] step.

Fig. 1C examines both steps on Cu(111) as a function of U.

On Cu(111) at U = -1 V<sub>RHE</sub>, the RDS for the HER is Heyrovsky, which leads to  $\Delta G^\ddagger = 0.79$  eV (0.16 eV lower than for C–C coupling) and to TOF = 0.32/s.

For Cu<sup>0</sup>/Cu<sub>2</sub>O at U = -1 V<sub>RHE</sub>, we find the RDS for the HER to be the Volmer reaction with  $\Delta G^\ddagger = 0.70$  eV, only -0.02 eV lower than C–C coupling.

Thus, the C<sub>2</sub> production rate is predicted to be comparable to HER rate on Cu<sup>0</sup>/Cu<sub>2</sub>O (0.39 times slower). Whereas on fully depleted Cu(111), the predicted rate for H<sub>2</sub> production is 479 times higher than C<sub>2</sub> production. The predicted ratio of the rate for H<sub>2</sub> production on Cu<sup>0</sup>/Cu<sub>2</sub>O versus fully depleted Cu(111) is  $3.14 \times 10^1$ . All atomic configurations for catalytic reactions are shown in SI Appendix, Figs. S6–S8.

To validate experimentally the above predictions from theory, we synthesized Cu-based catalysts through EC deposition of Cu<sub>2</sub>O on polycrystalline Cu. Compared to the planar surface of polycrystalline

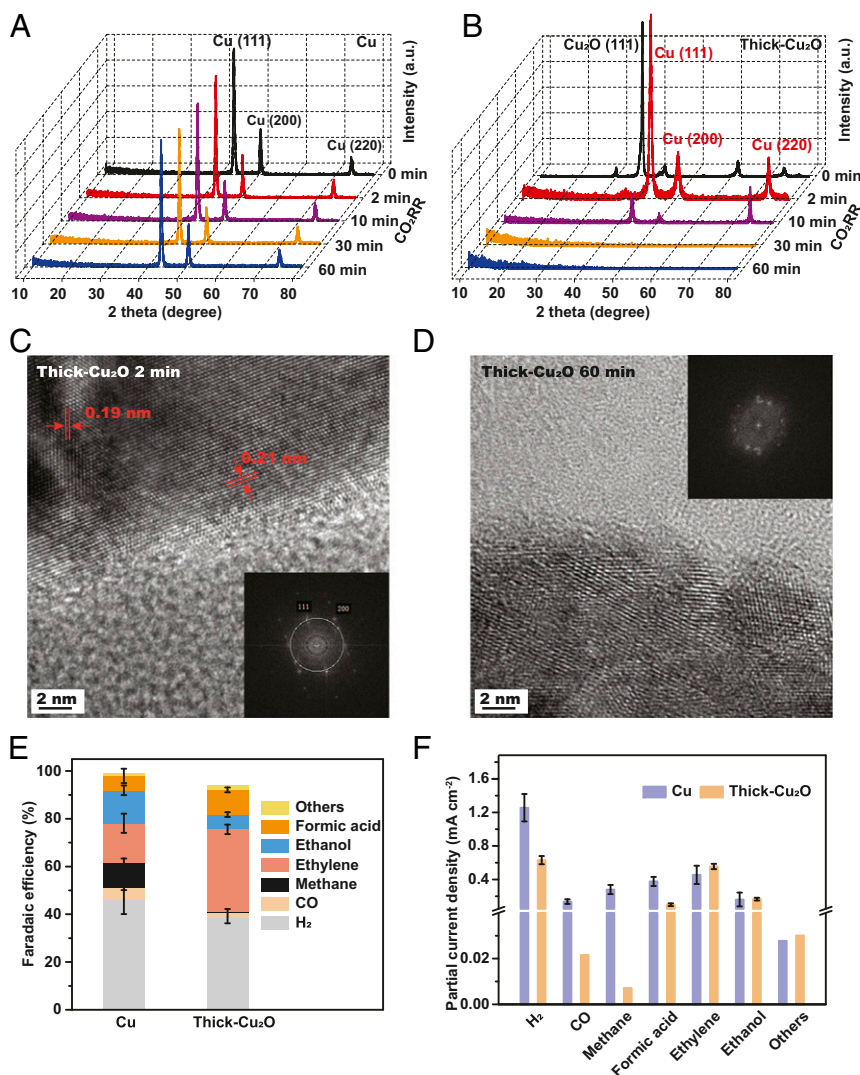


**Fig. 2.** Stable phases and catalytic activities of polycrystalline Cu and thick Cu<sub>2</sub>O under CO<sub>2</sub>RR. Ex situ GIXRD analysis of polycrystalline Cu (A) and thick Cu<sub>2</sub>O (B) after 0 (as-prepared), 2, 10, 30, and 60 min CO<sub>2</sub>RR at -1 V<sub>RHE</sub> in 0.1 M CO<sub>2</sub>-saturated K<sub>2</sub>CO<sub>3</sub> electrolyte (pH 7). High-resolution transmission electron microscopy images of thick Cu<sub>2</sub>O under CO<sub>2</sub>RR for 2 min (C) with corresponding fast Fourier transform (Inset) and 1 h (D) with corresponding fast Fourier transform (Inset); fragmented Cu-based nanoparticles with lower crystallinity were observed over 1 h CO<sub>2</sub>RR. (E) FEs of CO<sub>2</sub>RR toward H<sub>2</sub> (gray), CO (gold), methane (black), ethylene (pink), ethanol (blue), formic acid (orange), and others: acetate, ethylene glycol, and 1-propanol (yellow) for Cu and thick Cu<sub>2</sub>O at -1 V<sub>RHE</sub>. (F) Partial current densities toward H<sub>2</sub>, CO, methane, formic acid, ethylene, ethanol, and others: allyl alcohol; *n*-propanol, normalized by electrochemically active surface area over Cu (purple); and thick Cu<sub>2</sub>O (orange) for 1 h CO<sub>2</sub>RR at -1 V<sub>RHE</sub> in CO<sub>2</sub>-saturated 0.1 M K<sub>2</sub>CO<sub>3</sub> electrolyte (pH 7). Average values in E and F are based on triplicates, and the errors correspond to the SEM of data points from individual samples in SI Appendix, Table S3.

Cu, our synthesized Cu<sub>2</sub>O samples exhibit polycrystalline grains with a 1- $\mu$ m thickness (*SI Appendix, Fig. S9*), which we refer to as thick Cu<sub>2</sub>O.

Under bulk electrolysis at  $-1 V_{\text{RHE}}$  with CO<sub>2</sub>-saturated 0.1 M K<sub>2</sub>CO<sub>3</sub> electrolyte for 65 min, the crystalline structures of polycrystalline Cu featuring Cu(111) are retained, as shown in ex situ grazing incidence X-ray diffraction (GIXRD) analysis (*Fig. 2A*).

On the other hand, thick Cu<sub>2</sub>O is reduced to Cu<sup>0</sup> because of removal of lattice oxygen under CO<sub>2</sub>RR, leading to disordered Cu<sup>0</sup> surface over time, as demonstrated by ex situ GIXRD (*Fig. 2B*). Complementary high-resolution transmission electron microscopy confirms that the surface of thick Cu<sub>2</sub>O is readily reduced to crystalline Cu<sup>0</sup> after 2 min of CO<sub>2</sub>RR (*Fig. 2C*). Then, this crystalline surface evolves into fragmented and disordered Cu-based nanoparticles over 60 min CO<sub>2</sub>RR (*Fig. 2D*), in excellent agreement with GIXRD results. Control experiments further revealed that thick Cu<sub>2</sub>O became crystalline Cu<sup>0</sup> under N<sub>2</sub> saturation at  $-1 V_{\text{RHE}}$  and at less negative potentials ( $-0.6 V_{\text{RHE}}$  and  $-0.3 V_{\text{RHE}}$ ) under CO<sub>2</sub>RR for 1 h (*SI Appendix, Fig. S10*). Thus, these experimental observations verify that the theoretically predicted Cu(111) and disordered Cu<sup>0</sup>/Cu<sub>2</sub>O model are indeed the thermodynamically stable structure for polycrystalline Cu and thick Cu<sub>2</sub>O under CO<sub>2</sub>RR at  $-1 V_{\text{RHE}}$ .

The initial catalytic activity and selectivity of polycrystalline Cu and thick Cu<sub>2</sub>O catalysts toward CO<sub>2</sub>RR were examined over 1 h by gas chromatography and high-performance liquid chromatography in a two-compartment flow cell (*SI Appendix, Fig. S11*). Compared to polycrystalline Cu, we find that using thick Cu<sub>2</sub>O catalysts leads to lower selectivity of H<sub>2</sub> evolution, while selectivity toward C<sub>2</sub> (ethylene and ethanol) products over C<sub>1</sub> (CO, methane, and formic acid) products is higher (*Fig. 2E*), in agreement with previous reports (25, 26). In particular, the C<sub>2</sub>/C<sub>1</sub> ratio reaches a value of 5.9 on thick Cu<sub>2</sub>O, while that for polycrystalline Cu is only 0.8, based on the faradaic efficiencies (FEs) in *Fig. 2E*. In addition to FE, to understand the intrinsic activity toward each product, we further plotted partial current density, normalized by electrochemically active surface area, for polycrystalline Cu and thick Cu<sub>2</sub>O catalysts in *Fig. 2F*. These data highlight that the enhanced C<sub>2</sub>/C<sub>1</sub> ratio on thick Cu<sub>2</sub>O mainly stems from suppression of C<sub>1</sub> products, while similar rates of C<sub>2</sub> (ethylene and ethanol) products

were observed on polycrystalline Cu and thick Cu<sub>2</sub>O catalysts during the first hour of measurements. Previous studies have shown that the activity and selectivity of C<sub>2</sub> production on Cu are strongly dependent on the surface morphology and chemical composition (14, 17, 27).

To assess the role of surface morphology on Cu and thick Cu<sub>2</sub>O catalysts under operating conditions, we employed quasi-in situ EC atomic force microscopy (*Fig. 3*). Compared to as-prepared polycrystalline Cu (0 min), no dramatic topography change was observed on Cu under CO<sub>2</sub>RR with a constant R<sub>a</sub> ( $\sim 2$  nm) (*Fig. 3A–C*). On the other hand, EC fragmentation occurred on the thick Cu<sub>2</sub>O catalysts along with nanoparticles formation on Cu<sub>2</sub>O grains during the first 1 min of EC measurements (*Fig. 3D and E*). Afterward, the changes in topography remain small on thick Cu<sub>2</sub>O (*Fig. 3E and F*), leading to constant R<sub>a</sub> ( $\sim 21$  nm), which is 10 times of that of polycrystalline Cu. The sharp discrepancy in surface topography and roughness of polycrystalline Cu and thick Cu<sub>2</sub>O rules out the possibility that surface topography or roughness play a predominant role in the similar C<sub>2</sub> production rate on polycrystalline Cu and thick Cu<sub>2</sub>O.

As a result, we argue that a similar initial chemical composition in polycrystalline Cu and thick Cu<sub>2</sub>O is key to achieve the similar activity of ethylene production, as supported by the results during the first hour of activity of Cu and thick Cu<sub>2</sub>O samples (*Fig. 2*). Specifically, X-ray photoelectron spectroscopy (XPS) reveals that polycrystalline Cu initially possesses native oxide surface layers (*SI Appendix, Fig. S12*), as it is well known that Cu is readily oxidized in air (16). The coexistence of native surface oxygen and Cu<sup>0</sup> substrate makes the polycrystalline Cu surface similar to a very thin MEOM structure. Meanwhile, the disordered Cu<sup>0</sup> character was naturally formed on thick Cu<sub>2</sub>O under CO<sub>2</sub>RR, as shown in *Fig. 2B–D*. Thus, similar rates for C<sub>2</sub> products obtained on polycrystalline Cu and Cu<sub>2</sub>O during 1 h CO<sub>2</sub>RR can be interpreted by taking into account that MEOM structure of polycrystalline Cu and the disordered Cu<sup>0</sup> character of thick Cu<sub>2</sub>O share a similar kinetic barrier for C–C coupling, as mentioned earlier. However, as native oxygen on polycrystalline Cu is depleted under CO<sub>2</sub>RR at  $-1 V_{\text{RHE}}$ , the population of the thin MEOM structure will decrease rapidly over time. In addition, theoretical calculations suggest that disordered Cu<sup>0</sup> surface in thick Cu<sub>2</sub>O would ultimately

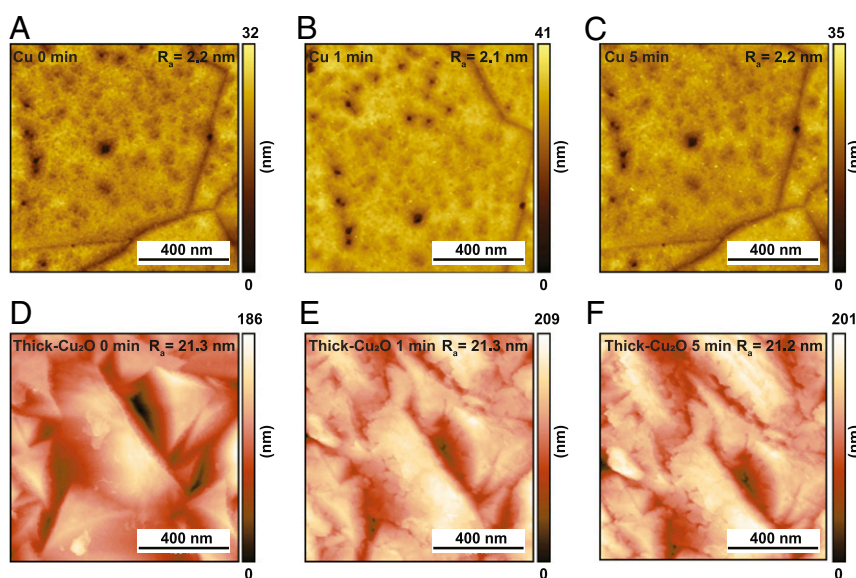


**Fig. 3.** Monitoring surface topography or roughness over Cu and thick Cu<sub>2</sub>O under CO<sub>2</sub>RR. Quasi-in situ EC-AFM images of polycrystalline Cu at 0 min (as-prepared) (A), 1 min (B), and 5 min (C) and thick Cu<sub>2</sub>O at 0 min (as-prepared) (D), 1 min (E), and 5 min (F) in 0.1 M CO<sub>2</sub>-saturated K<sub>2</sub>CO<sub>3</sub> electrolyte (pH 7) at  $-0.8 V_{\text{RHE}}$ .

stabilize to crystalline Cu<sup>0</sup> after oxygen is fully depleted. In this context, we consider that the long-term CO<sub>2</sub>RR selectivity and activity toward ethylene on polycrystalline Cu and Cu<sub>2</sub>O catalysts should be time dependent, which is associated with oxygen depletion. As residual oxygen is removed completely and disordered, Cu<sup>0</sup> transforms to pure crystalline Cu<sup>0</sup>, leading to H<sub>2</sub> as the dominant product, in excellent agreement with the predictions by the DFT calculations.

To validate this hypothesis, we further synthesized a thin Cu<sub>2</sub>O with 0.2- $\mu$ m thickness (*SI Appendix*, Fig. S13) to compare with the results for thick Cu<sub>2</sub>O. We proceeded to carry out long-term measurements (15 to 25 h) of product distributions on polycrystalline Cu, thin Cu<sub>2</sub>O, and thick Cu<sub>2</sub>O at  $-1 V_{\text{RHE}}$  with CO<sub>2</sub>-saturated 0.1 M K<sub>2</sub>CO<sub>3</sub> electrolyte. We monitored hourly gaseous ethylene and H<sub>2</sub> producing rates over time (Fig. 4), as well as the corresponding full products detection over the measured time (*SI Appendix*, Figs. S14 and S15). The total FEs are close to 100% for all samples.

As expected, selectivity and production rate of ethylene rapidly decayed on polycrystalline Cu catalyst within 1 h because of the depletion of native oxygen, while the HER rates increase with time. Furthermore, we employed a suit of characterizations including cyclic voltammetry, inductively coupled plasma mass spectrometry, and XPS analysis to exclude the role of surface texturing and metal ion contamination in determining the selectivity switch from ethylene to H<sub>2</sub> on polycrystalline Cu (*SI Appendix*, Figs. S16 and S17 and Table S4).

By contrast, the selectivity and production rate of ethylene on thin Cu<sub>2</sub>O and thick Cu<sub>2</sub>O slightly increased over the first 4 h, followed by a slow decay over time. Ultimately, C<sub>2</sub> production goes eventually to a level 1,600 times smaller than HER for polycrystalline Cu and 680 times lower for Cu<sub>2</sub>O catalysts, in excellent agreement with theory predictions. In particular, for all cases, ethylene production finally became negligible with sufficient time:  $\sim 4$  h for polycrystalline Cu,  $\sim 15$  h for thin Cu<sub>2</sub>O, and  $\sim 20$  h for thick Cu<sub>2</sub>O.

Moreover, we demonstrated that after 16 h CO<sub>2</sub>RR, polycrystalline Cu, thin Cu<sub>2</sub>O, and thick Cu<sub>2</sub>O catalysts were all able to recover their initial selectivity toward ethylene production: 92, 77, and 78% of their initial activity, respectively (Fig. 4G). This result was obtained by simply allowing the samples to regain a native oxide layer via reoxidization in the air.

Taking these results together, we conclude that the activity and selectivity of polycrystalline Cu and Cu<sub>2</sub>O catalysts toward ethylene are influenced dramatically by the oxygen content within the Cu-based catalysts.

This interpretation was further corroborated by angle-resolved XPS (AR-XPS) analysis over as-prepared polycrystalline Cu, Cu after 1 h CO<sub>2</sub>RR, and Cu after 16 h CO<sub>2</sub>RR (*SI Appendix*, Figs. S18–S20). To minimize the oxidation of the sample in air, the sample was rinsed, dried with N<sub>2</sub> flow, and transferred to the vacuum chamber of XPS within 2 min after the CO<sub>2</sub>RR measurements were completed. The O 1s spectra show that lattice oxygen decreases with increasing takeoff angle on both as-prepared polycrystalline Cu and Cu after 1 h CO<sub>2</sub>RR, indicating that subsurface lattice oxygen is present (28). In contrast, only surface-adsorbed OH/H<sub>2</sub>O is observed on polycrystalline Cu after 16 h CO<sub>2</sub>RR (*SI Appendix*, Fig. S18 and Table S5), which is consistent with Cu 2p and Cu Auger transition (Cu L<sub>3</sub>M<sub>4,5</sub>M<sub>4,5</sub>, *SI Appendix*, Figs. S19 and S20).

It is important to note that in situ Raman measurements at  $-1 V_{\text{RHE}}$  indicate that the total reduction of thick Cu<sub>2</sub>O was most likely completed in 1 h (*SI Appendix*, Fig. S21), which is shorter than the critical time for the selectivity switch from ethylene to H<sub>2</sub>, observed in Fig. 4. By contrast, we find that the time scale of the relaxation of disordered Cu<sup>0</sup> into crystalline Cu<sup>0</sup> is much longer than that one of Cu<sub>2</sub>O reduction, which agrees well with the time scale of the switch in selectivity (*SI Appendix*, Fig. S22). Thus, we propose that the lagging change on C<sub>2</sub> production, compared with

Cu<sub>2</sub>O reduction, is most likely due to the slow relaxation of disordered Cu<sup>0</sup> into crystalline Cu<sup>0</sup>. While Raman spectroscopy measurements exclude the presence of an underlayer of (partially reduced) Cu<sub>2</sub>O after 1 h, previous studies showed that disordered Cu<sup>0</sup> can have more labile oxygen in the lattice during CO<sub>2</sub>RR (6, 12). Moreover, Cuenya et al. suggested that the K<sup>+</sup> cation in the electrolyte may be able to retain the removal of subsurface oxygen species under CO<sub>2</sub>RR (29).

In addition, our theoretical calculations (*SI Appendix*, Fig. S4) find that the disordered Cu<sup>0</sup> relaxes back to Cu(111) after oxygen is fully depleted. While the relationship between slow crystalline relaxation and residue oxygen requires further investigations, the comparison of AR-XPS analysis over as-prepared thick Cu<sub>2</sub>O, thick Cu<sub>2</sub>O after 1 h, and after 16 h CO<sub>2</sub>RR (*SI Appendix*, Fig. S23 and Table S6) reveals that subsurface oxygen is observed on thick Cu<sub>2</sub>O after 1 h CO<sub>2</sub>RR but is absent after 16 h CO<sub>2</sub>RR. This result implies that residual oxygen is retained in the lattice, even after Cu<sub>2</sub>O was reduced.

These findings highlight the essential role of subsurface oxygen in C<sub>2</sub> production on Cu-based catalysts and how this role is related to inducing the formation of disordered Cu<sup>0</sup>. The disordered Cu<sup>0</sup> structure represents the thermodynamically stable structure of Cu<sub>2</sub>O-based catalysts under CO<sub>2</sub>RR, which substantially enhances intrinsic C<sub>2</sub> production, compared to pure crystalline Cu<sup>0</sup>. This phase is achieved by dynamic transformation of Cu-based nanocrystals under CO<sub>2</sub>RR conditions (6, 30).

While previous studies on subsurface oxygen on Cu demonstrate that subsurface oxygen may not play an essential role in CO<sub>2</sub> adsorption (31), Nilsson and coworkers show that subsurface oxygen on Cu is instrumental in enhancing CO adsorption, which can lead to an improved C<sub>2</sub> selectivity (32, 33).

We calculate C<sub>2</sub> and HER TOFs on various Cu-based models. These results demonstrate that the presence of residual oxygen is essential for retention and long-term stability of the disordered Cu<sup>0</sup> surface that is active toward C<sub>2</sub> production. This finding can explain why disordered Cu-based catalysts and uncoordinated Cu sites at grain boundaries have higher selectivity for C<sub>2</sub> products (6, 8, 34). Thus, allowing the residual oxygen of Cu catalysts to be replenished from other robust oxides under CO<sub>2</sub>RR might be a promising direction to design efficient CO<sub>2</sub>RR catalysts with sustained C<sub>2</sub> selectivity. Additionally, the intrinsic ability of Cu to be rapidly oxidized in the air to regain its catalytic ability is beneficial to developing a sustainable/recyclable catalyst. For example, recent findings show that the continuous regeneration of defects and Cu<sup>+</sup> species favors C–C coupling pathways (14).

In summary, we provide mechanistic insights into C<sub>2</sub> production over Cu-based catalysts by GCP-K DFT calculations, showing that for pure Cu(111) with no subsurface oxygen, the rate of C<sub>2</sub> production is  $\sim 500$  times smaller than HER, whereas reduced models starting with Cu<sub>2</sub>O led to C<sub>2</sub> production  $\sim 10,000$  times faster. Furthermore, we combine time-dependent product detection with a correlative characterization approach to confirm that activity and selectivity of polycrystalline Cu and Cu<sub>2</sub>O catalysts toward ethylene is determined by the disordered Cu<sup>0</sup> character involving oxygen content within Cu-based catalysts. Compared to the MEOM structure, the formation of a disordered Cu<sup>0</sup> surface induced by the removal of lattice oxygen from Cu<sub>2</sub>O is thermodynamically favorable under CO<sub>2</sub>RR. After long-term CO<sub>2</sub>RR, pure crystalline Cu<sup>0</sup> without subsurface oxygen leads only to HER at  $-1 V_{\text{RHE}}$  in aqueous solutions, in excellent agreement with the DFT calculations. Based on this theoretical and experimental understanding, we conclude that the key for the rational development of highly active electrocatalysts toward C<sub>2</sub> production is to modify the catalyst conditions in such a way as to preserve surface or subsurface oxygen in the Cu catalyst under CO<sub>2</sub>RR conditions.

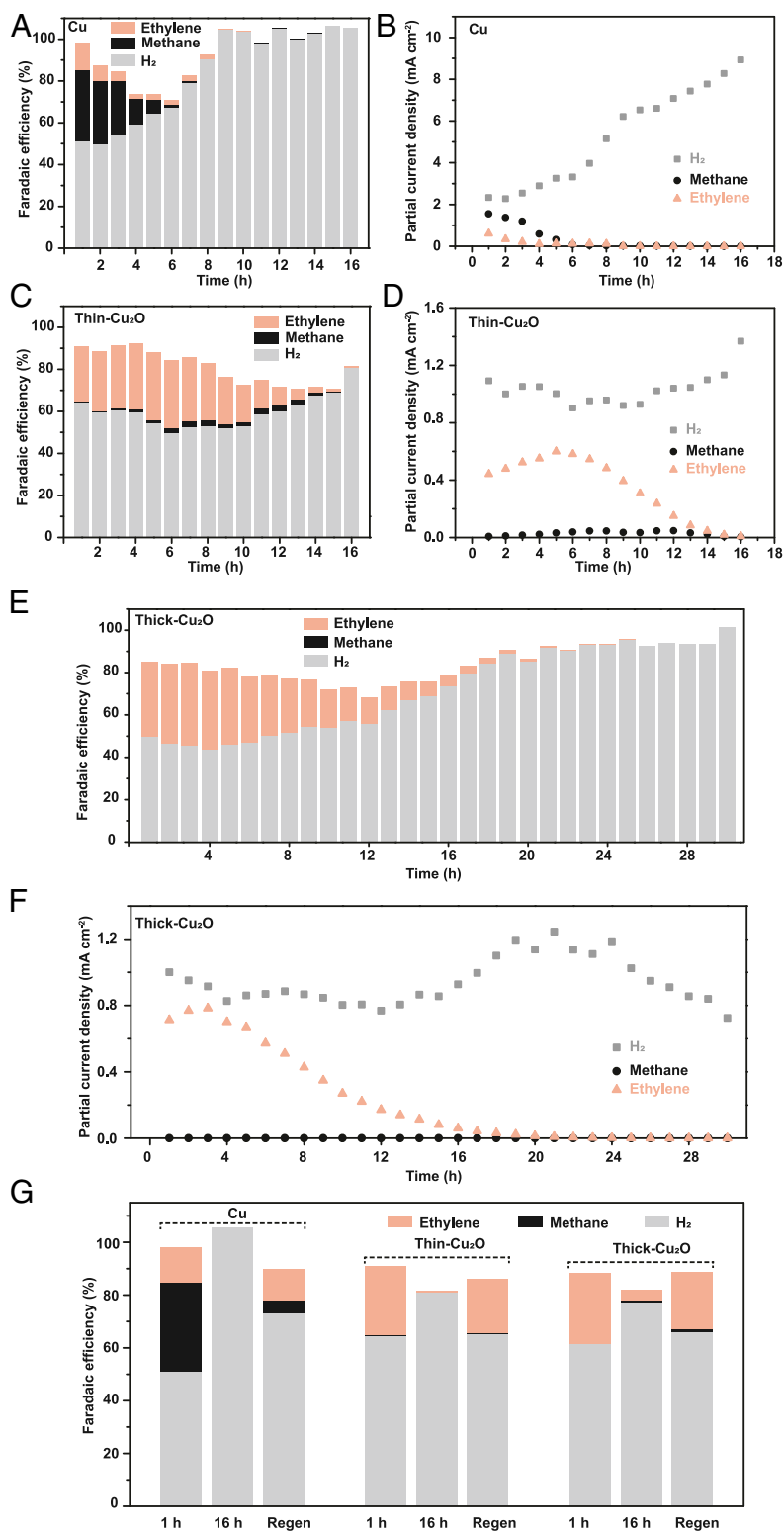


**Fig. 4.** Long-term CO<sub>2</sub>RR measurements on polycrystalline Cu, thin Cu<sub>2</sub>O, and thick Cu<sub>2</sub>O. (A) FE of polycrystalline Cu; (B) partial current densities of polycrystalline Cu toward H<sub>2</sub>, methane, and ethylene, normalized by electrochemically active surface area (ECSA); (C) FE of thin Cu<sub>2</sub>O; (D) partial current densities of thin Cu<sub>2</sub>O, toward H<sub>2</sub>, methane, and ethylene, normalized by ECSA; (E) FE of thick Cu<sub>2</sub>O; (F) partial current densities of thick Cu<sub>2</sub>O, toward H<sub>2</sub>, methane, and ethylene, normalized by ECSA at  $-1.0 V_{RHE}$  in CO<sub>2</sub>-saturated 0.1 M K<sub>2</sub>CO<sub>3</sub> electrolyte (pH 7) for CO<sub>2</sub>RR over time. (G) FE of Cu, thin Cu<sub>2</sub>O, and thick Cu<sub>2</sub>O at  $-1.0 V_{RHE}$  in CO<sub>2</sub>-saturated 0.1 M K<sub>2</sub>CO<sub>3</sub> electrolyte (pH 7) after 1 h CO<sub>2</sub>RR, 16 h CO<sub>2</sub>RR, and Cu, thin Cu<sub>2</sub>O and thick Cu<sub>2</sub>O experienced 16 h CO<sub>2</sub>RR, followed by a regeneration process: allowing the above catalysts to sit in air for about 2 wk.

## Materials and Methods

**Electrodeposition of Cu<sub>2</sub>O.** In a typical experiment, a 0.4 M Cu sulfate pentahydrate solution was used as the plating solution, prepared by stirring 4.99 g CuSO<sub>4</sub>·5 H<sub>2</sub>O in 50 mL MilliQ water. A total of 3 M (13.51 g) lactic acid was added to stabilize Cu<sup>2+</sup> in basic solution, and then, 3 M NaOH was added to the solution until the pH of plating solution reached 12. Thick Cu<sub>2</sub>O and thin Cu<sub>2</sub>O were deposited on Cu foils (99.999%, Alfa Aesar) for 150 and 15 min, respectively, at a constant current density (−0.1 mA/cm<sup>2</sup>) in a three-electrode configuration under room temperature. To obtain a uniform coating, the Cu foil was mechanically polished with sandpapers (1,200 g Wetordry sandpaper, 3 M) and electropolished in 85% phosphoric acid at +2.1 V for 5 min, followed by annealing in air at 300 °C for 30 min prior to use. After the deposition, the sample was gently rinsed with MilliQ water and then dried with a nitrogen gun.

**Product Detection.** EC experiments were conducted in a two-compartment flow cell fabricated from polyether ether ketone. A Selemion anion-exchange membrane separated the two chambers. A Pt foil was used as the counter electrode. A leak-free Ag/AgCl electrode (LF-1, 1-mm outer diameter, Innovative Instruments, Inc.) was used as the reference electrode.

**Computational Details.** Our DFT calculations used the Vienna ab initio simulation package (VASP) (35, 36) with the VASPsol solvation model (37) for geometry optimization, followed by single-point calculations using the charge-asymmetric nonlocally determined local-electric solvation model (CANDLE) (38), as incorporated in the joint density-functional theory (JDFTx) (39).

The electron exchange and correlation were treated within the generalized gradient approximation (40) in the form of the Perdew–Burke–Ernzerhof functional, including the D3 correction for London Dispersion (van der Waals attraction) (41). The interaction between the ionic core and the valence electrons was described by the projector-augmented wave method (42). We used a plane-wave basis up to an energy cutoff of 500 eV. The Brillouin zone was sampled using the 3 × 3 × 1 Monkhorst–Pack grid (43). The convergence criteria for the electronic structure and the atomic geometry were 10<sup>−5</sup> eV and 0.03 eV/Å for initial state (IS) and final state (FS) and 0.01 eV/Å for TS, respectively. We exploited the variational transition state (TS) theory package to search the TS using both climbing-image nudged elastic band method (44) and the dimer method for TS search (45).

The Gibbs free energies were calculated at 298 K and 1 atm as the following:

$$G = H - T\Delta S = E_{DFT} + E_{ZPE} + E_{solv} + \int_0^{298} C_v dT - T\Delta S,$$

where  $E_{DFT}$  is the total energy,  $E_{ZPE}$  is zero-point vibrational energy,  $E_{solv}$  is

the solvation energy,  $\int_0^{298} C_v dT$  is the enthalpy, and  $\Delta S$  is the change in entropy. The turnover frequency (TOF) of a reaction is given by

$$\text{TOF} = \frac{k_B T}{h} \exp\left(-\frac{\Delta G^\ddagger}{k_B T}\right) [1/s],$$

where  $k_B$  is the Boltzmann constant,  $T$  is the room temperature (298 K),  $h$  is the Planck's constant, and  $\Delta G^\ddagger$  is a free energy barrier.

The Cu(111) system was described by four layers of 4 × 4 supercell with two bottom layers fixed. Pristine Cu<sub>2</sub>O and oxide-derived Cu were described by four trilayers of 4 × 4 supercell with two bottom trilayers fixed. The model system was described by three layers of 4 × 4 Cu slab with 20 Å of vacuum. The bottom two layers are fixed. All designed models have > 20 Å vacuum.

**H<sub>2</sub> and C<sub>2</sub> Production on Cu MEOM Model.** In a previous study, we suggested that the MEOM model's surface has adjacent-oxidized and metallic regions (9). On MEOM, we predict that C–C coupling has a kinetic barrier of 0.71 eV, which is 0.4 eV lower compared to that on Cu(111). We showed that the enhancement of C–C coupling on this catalyst is due to the attractive electrostatics, involving a carbon on the positively charge Cu<sup>+</sup> induced by subsurface oxygen next to a C bound to a Cu<sup>0</sup> site.

In our calculation on this MEOM catalyst using the GCP-K method, we find that C–C coupling has a kinetic barrier of  $\Delta G^\ddagger = 0.72$  eV, while the RDS for HER (the Heyrovsky reaction) has a barrier of  $\Delta G^\ddagger = 1.02$  eV. This leads to a C<sub>2</sub>/H<sub>2</sub> ratio of 1.23 × 10<sup>6</sup>. Compared to Cu(111), C–C coupling is 7.03 × 10<sup>3</sup> times faster, but HER is 1.19 × 10<sup>−4</sup> times slower.

All configurations for IS, TS, and FS of C–C coupling and Volmer and Heyrovsky reactions are depicted in *SI Appendix, Figs. S6–S8*.

**Data Availability.** All study data are included in the article and/or *SI Appendix*.

**ACKNOWLEDGMENTS.** This study is based on work initiated with funding from the Joint Center for Artificial Photosynthesis, a Department of Energy (DOE) Energy Innovation Hub, supported through the Office of Science of the US DOE under Award DE-SC0004993 and completed with funding from the Liquid Sunlight Alliance (LISA), which is supported by the US DOE, Office of Science, Office of Basic Energy Sciences, Fuels from Sunlight Hub under Award DE-SC0021266. Raman spectroscopy and some of the theoretical calculations were specifically supported by LISA. Work at the Molecular Foundry was supported by the Office of Science, Office of Basic Energy Sciences, of the US DOE under Contract No. DE-AC02-05CH11231. These studies used the Extreme Science and Engineering Discovery Environment which is supported by National Science Foundation Grant ACI-1548562.

- C. F. Shih, T. Zhang, J. Li, C. Bai, Powering the future with liquid sunshine. *Joule* **2**, 1925–1949 (2018).
- P. De Luna *et al.*, What would it take for renewably powered electrosynthesis to displace petrochemical processes? *Science* **364**, eaav3506 (2019). Correction in: *Science* **367**, eabb092 (2020).
- M. B. Ross *et al.*, Designing materials for electrochemical carbon dioxide recycling. *Nat. Catal.* **2**, 648–658 (2019).
- S. Nitopi *et al.*, Progress and perspectives of electrochemical CO<sub>2</sub> reduction on copper in aqueous electrolyte. *Chem. Rev.* **119**, 7610–7672 (2019).
- P. De Luna *et al.*, Catalyst electro-redeposition controls morphology and oxidation state for selective carbon dioxide reduction. *Nat. Catal.* **1**, 103–110 (2018).
- H. Jung *et al.*, Electrochemical fragmentation of Cu<sub>2</sub>O nanoparticles enhancing selective C–C coupling from CO<sub>2</sub> reduction reaction. *J. Am. Chem. Soc.* **141**, 4624–4633 (2019).
- H. Mistry *et al.*, Highly selective plasma-activated copper catalysts for carbon dioxide reduction to ethylene. *Nat. Commun.* **7**, 12123 (2016). Correction in: *Nat. Commun.* **7**, 12945 (2016).
- C. W. Li, M. W. Kanan, CO<sub>2</sub> reduction at low overpotential on Cu electrodes resulting from the reduction of thick Cu<sub>2</sub>O films. *J. Am. Chem. Soc.* **134**, 7231–7234 (2012).
- H. Xiao, W. A. Goddard III, T. Cheng, Y. Liu, Cu metal embedded in oxidized matrix catalyst to promote CO<sub>2</sub> activation and CO dimerization for electrochemical reduction of CO<sub>2</sub>. *Proc. Natl. Acad. Sci. U.S.A.* **114**, 6685–6688 (2017).
- D. Gao *et al.*, Plasma-activated copper nanocube catalysts for efficient carbon dioxide electroreduction to hydrocarbons and alcohols. *ACS Nano* **11**, 4825–4831 (2017).
- S. Y. Lee *et al.*, Mixed copper states in anodized Cu electrocatalyst for stable and selective ethylene production from CO<sub>2</sub> reduction. *J. Am. Chem. Soc.* **140**, 8681–8689 (2018).
- P.-P. Yang *et al.*, Protecting copper oxidation state via intermediate confinement for selective CO<sub>2</sub> electroreduction to C<sub>2</sub>+ fuels. *J. Am. Chem. Soc.* **142**, 6400–6408 (2020).
- M. Favaro *et al.*, Subsurface oxide plays a critical role in CO<sub>2</sub> activation by Cu(111) surfaces to form chemisorbed CO<sub>2</sub>, the first step in reduction of CO<sub>2</sub>. *Proc. Natl. Acad. Sci. U.S.A.* **114**, 6706–6711 (2017).
- R. M. Arán-Ais, F. Scholten, S. Kunze, R. Rizo, B. Roldan Cuenya, The role of in situ generated morphological motifs and Cu(I) species in C<sub>2</sub> product selectivity during CO<sub>2</sub> pulsed electroreduction. *Nat. Energy* **5**, 317–325 (2020).
- L. Mandal *et al.*, Investigating the role of copper oxide in electrochemical CO<sub>2</sub> reduction in real time. *ACS Appl. Mater. Interfaces* **10**, 8574–8584 (2018).
- Y. Lum, J. W. Ager, Stability of residual oxides in oxide-derived copper catalysts for electrochemical CO<sub>2</sub> reduction investigated with <sup>18</sup>O labeling. *Angew. Chem. Int. Ed. Engl.* **57**, 551–554 (2018).
- K. Jiang *et al.*, Effects of surface roughness on the electrochemical reduction of CO<sub>2</sub> over Cu. *ACS Energy Lett.* **5**, 1206–1214 (2020).
- Y. Huang, R. J. Nielsen, W. A. Goddard III, Reaction mechanism for the hydrogen evolution reaction on the basal plane sulfur vacancy site of MoS<sub>2</sub> using grand canonical potential kinetics. *J. Am. Chem. Soc.* **140**, 16773–16782 (2018).
- A. A. Peterson, F. Abild-Pedersen, F. Studt, J. Rossmeisl, J. K. Nørskov, How copper catalyzes the electroreduction of carbon dioxide into hydrocarbon fuels. *Energy Environ. Sci.* **3**, 1311–1315 (2010).
- X. Nie, M. R. Esopi, M. J. Janik, A. Asthagiri, Selectivity of CO<sub>2</sub> reduction on copper electrodes: The role of the kinetics of elementary steps. *Angew. Chem. Int. Ed. Engl.* **52**, 2459–2462 (2013).
- F. Calle-Vallejo, M. T. M. Koper, Theoretical considerations on the electroreduction of CO to C<sub>2</sub> species on Cu(100) electrodes. *Angew. Chem. Int. Ed. Engl.* **52**, 7282–7285 (2013).
- X. Nie, W. Luo, M. J. Janik, A. Asthagiri, Reaction mechanisms of CO<sub>2</sub> electrochemical reduction on Cu(111) determined with density functional theory. *J. Catal.* **312**, 108–122 (2014).
- W. Luo, X. Nie, M. J. Janik, A. Asthagiri, Facet dependence of CO<sub>2</sub> reduction paths on Cu electrodes. *ACS Catal.* **6**, 219–229 (2016).
- T. Cheng, H. Xiao, W. A. Goddard III, Full atomistic reaction mechanism with kinetics for CO reduction on Cu(100) from ab initio molecular dynamics free-energy calculations at 298 K. *Proc. Natl. Acad. Sci. U.S.A.* **114**, 1795–1800 (2017).

Liu *et al.*

CO<sub>2</sub> reduction on pure Cu produces only H<sub>2</sub> after subsurface O is depleted: Theory and experiment

PNAS | 7 of 8

<https://doi.org/10.1073/pnas.2012649118>

25. R. Kas *et al.*, Electrochemical CO<sub>2</sub> reduction on Cu<sub>2</sub>O-derived copper nanoparticles: Controlling the catalytic selectivity of hydrocarbons. *Phys. Chem. Chem. Phys.* **16**, 12194–12201 (2014).
26. Y. Lum, B. Yue, P. Lobaccaro, A. T. Bell, J. W. Ager, Optimizing C–C coupling on oxide-derived copper catalysts for electrochemical CO<sub>2</sub> reduction. *J. Phys. Chem. C* **121**, 14191–14203 (2017).
27. C.-T. Dinh *et al.*, CO<sub>2</sub> electroreduction to ethylene via hydroxide-mediated copper catalysis at an abrupt interface. *Science* **360**, 783–787 (2018).
28. A. Eilert *et al.*, Subsurface oxygen in oxide-derived copper electrocatalysts for carbon dioxide reduction. *J. Phys. Chem. Lett.* **8**, 285–290 (2017).
29. D. Gao *et al.*, Activity and selectivity control in CO<sub>2</sub> electroreduction to multicarbon products over CuO<sub>x</sub> catalysts via electrolyte design. *ACS Catal.* **8**, 10012–10020 (2018).
30. Y. Li *et al.*, Electrochemically scrambled nanocrystals are catalytically active for CO<sub>2</sub>-to-multicarbon. *Proc. Natl. Acad. Sci. U.S.A.* **117**, 9194–9201 (2020).
31. A. J. Garza, A. T. Bell, M. Head-Gordon, Is subsurface oxygen necessary for the electrochemical reduction of CO<sub>2</sub> on copper? *J. Phys. Chem. Lett.* **9**, 601–606 (2018).
32. F. Cavalca *et al.*, Nature and distribution of stable subsurface oxygen in copper electrodes during electrochemical CO<sub>2</sub> reduction. *J. Phys. Chem. C* **121**, 25003–25009 (2017).
33. A. Eilert, F. S. Roberts, D. Friebel, A. Nilsson, Formation of copper catalysts for CO<sub>2</sub> reduction with high ethylene/methane product ratio investigated with in situ X-ray absorption spectroscopy. *J. Phys. Chem. Lett.* **7**, 1466–1470 (2016).
34. Y. Huang, Y. Chen, T. Cheng, L.-W. Wang, W. A. Goddard, Identification of the selective sites for electrochemical reduction of CO to C<sub>2+</sub> products on copper nanoparticles by combining reactive force fields, density functional theory, and machine learning. *ACS Energy Lett.* **3**, 2983–2988 (2018).
35. G. Kresse, J. Hafner, Ab initio molecular-dynamics simulation of the liquid-metal-amorphous-semiconductor transition in germanium. *Phys. Rev. B Condens. Matter* **49**, 14251–14269 (1994).
36. G. Kresse, J. Furthmüller, Efficient iterative schemes for ab initio total-energy calculations using a plane-wave basis set. *Phys. Rev. B Condens. Matter* **54**, 11169–11186 (1996).
37. K. Mathew, R. Sundararaman, K. Letchworth-Weaver, T. A. Arias, R. G. Hennig, Implicit solvation model for density-functional study of nanocrystal surfaces and reaction pathways. *J. Chem. Phys.* **140**, 084106 (2014).
38. R. Sundararaman, W. A. Goddard III, The charge-asymmetric nonlocally determined local-electric (CANDLE) solvation model. *J. Chem. Phys.* **142**, 064107 (2015).
39. R. Sundararaman *et al.*, JDFTx: Software for joint density-functional theory. *SoftwareX* **6**, 278–284 (2017).
40. J. P. Perdew, K. Burke, M. Ernzerhof, Generalized gradient approximation made simple. *Phys. Rev. Lett.* **77**, 3865–3868 (1996).
41. E. R. Johnson, A. D. Becke, A post-Hartree-Fock model of intermolecular interactions: Inclusion of higher-order corrections. *J. Chem. Phys.* **124**, 174104 (2006).
42. P. E. Blöchl, Projector augmented-wave method. *Phys. Rev. B Condens. Matter* **50**, 17953–17979 (1994).
43. H. J. Monkhorst, J. D. Pack, Special points for Brillouin-zone integrations. *Phys. Rev. B* **13**, 5188–5192 (1976).
44. G. Henkelman, B. P. Uberuaga, H. Jónsson, A climbing image nudged elastic band method for finding saddle points and minimum energy paths. *J. Chem. Phys.* **113**, 9901–9904 (2000).
45. G. Henkelman, H. Jónsson, A dimer method for finding saddle points on high dimensional potential surfaces using only first derivatives. *J. Chem. Phys.* **111**, 7010–7022 (1999).